

Jiří Jan; Radim Kolář; Libor Kubečka; Jan Odstrčilík; Jiří Gazárek  
Fusion based analysis of ophthalmologic image data

*Kybernetika*, Vol. 47 (2011), No. 3, 455--481

Persistent URL: <http://dml.cz/dmlcz/141596>

## Terms of use:

© Institute of Information Theory and Automation AS CR, 2011

Institute of Mathematics of the Academy of Sciences of the Czech Republic provides access to digitized documents strictly for personal use. Each copy of any part of this document must contain these *Terms of use*.



This paper has been digitized, optimized for electronic delivery and stamped with digital signature within the project *DML-CZ: The Czech Digital Mathematics Library* <http://project.dml.cz>

## FUSION BASED ANALYSIS OF OPHTHALMOLOGIC IMAGE DATA

JIŘÍ JAN, RADIM KOLÁŘ, LIBOR KUBEČKA, JAN ODSTRČILÍK AND JIŘÍ GAZÁREK

The paper presents an overview of image analysis activities of the Brno DAR group in the medical application area of retinal imaging. Particularly, illumination correction and SNR enhancement by registered averaging as preprocessing steps are briefly described; further mono- and multimodal registration methods developed for specific types of ophthalmological images, and methods for segmentation of optical disc, retinal vessel tree and autofluorescence areas are presented. Finally, the designed methods for neural fibre layer detection and evaluation on retinal images, utilising different combined texture analysis approaches and several types of classifiers, are shown. The results in all the areas are shortly commented on at the respective sections. In order to emphasise methodological aspects, the methods and results are ordered according to consequential phases of processing rather than divided according to individual medical applications.

*Keywords:* image fusion, image analysis, 2D and 3D image registration, ophthalmology, retina imaging, subtractive angiography, computed tomography, illumination correction, image averaging, spatial transforms

*Classification:* 93E12, 62A10

### 1. INTRODUCTION

This paper provides a brief overview of the retinal image analysis activities of Brno group working in frame of the research centre DAR (Data, Algorithms, Decision making) coordinated by the Institute of Information Theory and Automation, Academy of Sciences of the Czech Republic. The activities concerning ophthalmological applications of image analysis were initiated by scientific contacts with the Erlangen university (Germany) already around 2000 [21]; here, the DAR-team activities performed during the first DAR period (2005–2009) will be summarised.

There are several modalities nowadays available for imaging the interior of eye – primarily the most common and widely accessible optical wide-angle fundus camera imaging the retina, with many diagnostically important details (nerve bundle terminal, so called optical disc (OD), vessel tree, macula, faintly also neural fibre layer (NFL), possibly deceased areas of different kind, etc.), [8, 12]. Another today important modality is the laser scanning tomography (LST) [27] providing 3D data on the eye interior. This has a possibility to use different laser wavelengths thus enabling, besides the most common infrared examination also excitation by blue laser light

leading then to autofluorescence phenomena that have been recognised to have also diagnostic importance. 2D projections of LST data are similar to fundus camera images, though carrying different information. Fusion of both these modalities brings then an important enhancement to possibilities of detecting diagnostically important features. Increasingly important is the new modality of optical coherence tomography (OCT) [3], which enables to image depth scans of the eye interior, primarily of the cross-sectional profiles of the retina, thus providing the objective evaluation of the retinal layers, particularly of the thickness of the neural fibre layer. This offers, during direct measurement on individual patients (though still expensive and not widely available), the objective assessment of the estimates of the NFL status provided for the same patients in the fundus camera images. The image material from all these modalities was provided for our group by the cooperating ophthalmological institutions – the university eye clinic in Erlangen (Germany) and the outpatient eye clinic in Zlin (Czech Republic). The task of the DAR team was generally to increase the diagnostic potential of the data by finding suitable ways of processing or analyse the data with the aim to support the medical diagnostics, and – in some cases – to enable even mass screening via automating some steps that are so far too time consuming, complex or tiresome for the medical experts to be applied in mass scale. The results were concurrently summarised in [22, 23, 24].

Several medically defined problem areas were namely treated: first registration and fusion of fundus camera images with the 2D LST images and consequently the optical disc segmentation, possibly allowing conclusions on OD deformations symptomatic for certain diseases. Another problem was segmentation of the vessel tree on retinal fundus camera images, necessary as a preliminary step before neural fibre layer (NFL) detection but also more generally useful. Another segmentation task was autofluorescence (AF) areas detection and evaluation. Finally, the status and contributions to the still very topical problem of detecting and evaluating the NFL, substantial for early glaucoma diagnosis, is described.

With respect to the overview character of the paper, the discussion of results and indications of possible future research are generally only very brief and are included at the respective partial sections in the main body of the paper in chapter 2. Considering this character, also other problem areas worked on by the Brno DAR-group should be mentioned: subtractive CT angiography aiming at substantial improvement of vessels presentation in time series of 3D CT data, 3D image synthesis in ultrasonic transmissive computed tomography (USCT) and fMRI image data analysis for neuroscience applications.

## 2. METHODOLOGY AND APPLICATIONS

The methods and results, obtained in the period 2005–2009 in the area of ophthalmologic application, are described in this chapter. Although they deal with the medically defined problems as mentioned in the Introduction, they are organised here differently to emphasise the methodological aspect – starting from preprocessing stage, via registration and segmentation to classification of derived features. Except preprocessing, the other stages utilise the fusion aspect in a certain degree, more or less explicitly described. The fusion may concern multimodal data, or monomodal data in time series, or both.

## 2.1. Pre-processing of retinal images

Most of the processed image data require a certain degree of pre-processing before they may be submitted to the fusion procedures. Mostly simple corrections are needed, like histogram based contrast adjustment, certain degree of convolution processing e.g. for edge enhancement etc. but in some cases, more sophisticated and not readily available procedures are needed; in these cases applying original approaches is necessary. Among them, an interesting problem was correcting the uneven illumination of retina when imaged by fundus camera. Although illumination correction has already been extensively treated in literature namely for MRI images, e.g. [2, 10, 17, 48, 66, 71], the retinal problem turned out specific [6]; and compared to MRI it required novel modifications as described in [40].

There, a method for correction of non-homogeneous illumination is presented, based on optimization of a shading model (called here the *bias field*, reflecting the terminology commonly used in processing of magnetic resonance (MR) images) with respect to Shannon's entropy. The evaluation of Shannon's entropy is based [53] on Parzen windowing method using spline-based shading model, which leads to expressing the derivatives of the entropy criterion analytically, thus enabling efficient use of gradient based optimization algorithms. The acquisition model (1) of image  $s(\mathbf{x})$  supposes the multiplicative illumination model  $b(\mathbf{x})$ ,

$$s(\mathbf{x}) = [(\rho(\mathbf{x}) + n_{tiss}(\mathbf{x}))b(\mathbf{x})] * h(\mathbf{x}) + n(\mathbf{x}) \approx o(\mathbf{x})b(\mathbf{x}) + n(\mathbf{x}) \quad (1)$$

where  $n(\mathbf{x})$  is external noise,  $n_{tiss}(\mathbf{x})$  represents the useful texture around the local mean  $\rho(\mathbf{x})$  corresponding to a particular type of tissue and  $h(\mathbf{x})$  is the impulse response of the imaging system. In the right hand side simplification,  $o(\mathbf{x})$  is the ideal image. Obviously, when the disturbances other than uneven illumination may be neglected (which is the case), the image can be estimated as

$$\hat{o}(\mathbf{x}) = \frac{s(\mathbf{x})}{\hat{b}(\mathbf{x}|\Phi)} - \frac{n(\mathbf{x})}{\hat{b}(\mathbf{x}|\Phi)} \approx \frac{s(\mathbf{x})}{\hat{b}(\mathbf{x}|\Phi)} \quad (2)$$

where  $\Phi$  is the to be determined vector of parameters controlling the illumination bias model. This model is based on extension of the Likar's et al. approach [49], applying the modified algorithm for retrospective shading correction to retinal images. The optimisation aiming at determining the optimum  $\Phi$  is then based on a quality criterion of illumination compensation based on Shannon's entropy and on Parzen windowing probability estimation. The idea is that the illumination represents additional information added to the information of the original signal  $o(\mathbf{x})$  and as the illumination bias is to be removed, the information content of the corrected image should be lower than that of the distorted image  $s(\mathbf{x})$ . Therefore, the Shannon's entropy  $H(\cdot)$  of the resulting image  $\hat{o}(\mathbf{x})$ ,

$$H = - \sum_k P(k) \log(P(k)), \quad (3)$$

where  $P(k)$  is the probability of intensity  $k$  appearing at any  $\mathbf{x}$  of the area  $\Omega$  of the  $\hat{o}(\mathbf{x})$ , should be minimized. Although  $k$  is a discrete variable, it may be well

approximated by a continuous variable  $\kappa$  with a probability density  $p(\kappa)$ . Then, in order to analytically derive the derivatives of the criterion, we may assume that the amount of information can be described by the integral version of (3),

$$H = - \int_{\kappa} p(\kappa) \log(p(\kappa)) d\kappa. \quad (4)$$

However, the probability density  $p(\kappa)$  is not available explicitly and must be estimated from the image data corrected by the bias estimate with the current parameters  $\Phi$ , providing that the image has been generated by a homogeneous stochastic field. For this purpose, the Parzen windows technique [53] has been used, in principle using the information contained in the intensity histogram of the image. The probability density is thus estimated from intensity samples  $\hat{o}(\mathbf{x}; \Phi)$  of the transformed image as

$$p(\kappa, \Phi) = \frac{1}{\Theta} \sum_{\mathbf{x} \in \Omega} \beta^{(3)} \left( \frac{\hat{o}(\mathbf{x}; \Phi) - \kappa}{z} \right), \quad (5)$$

where  $\beta^{(3)}$  is  $3^{rd}$  order B-spline kernel of the model,  $z$  is the parameter analogue to histogram bin size and  $\Theta$  is a normalization coefficient assuring the integral of  $p(\kappa)$  being equal to 1. For the derivatives of the criterion it is thus obtained

$$\frac{\partial H(\kappa; \Phi)}{\partial \Phi_k} \approx - \sum_k \frac{\partial p(\kappa; \Phi)}{\partial \Phi_k} (\log(p(\kappa; \Phi)) + 1). \quad (6)$$

This approach allows, as a novelty, to derive analytical expressions for derivatives of this criterion with respect to parameters of the used B-spline multiplicative illumination model, which ease substantially the optimization calculations compared to purely numerical evaluation of derivatives.

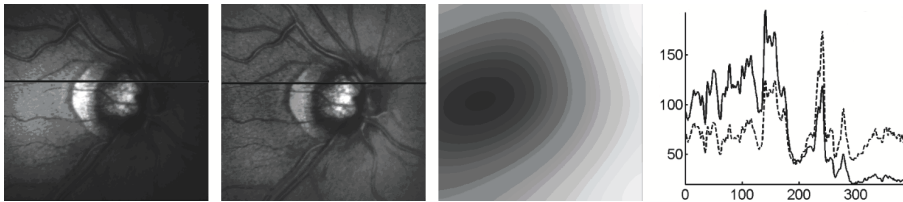


**Fig. 1.** From left: retinal image highly corrupted by non-homogeneous illumination, image after multiplicative correction by recovered bias field, the obtained normalized bias field controlled by  $3 \times 3$  spline parameters, intensity profiles along the indicated row before and after correction.

Among the tested optimizers, the gradient based optimizer with varying step has shown to have the fastest and most precise convergence to the criterion optimum. The designed algorithm proved to suppress approximately 70% of the artificially introduced non-homogeneous illumination. Consequently, the method was qualitatively tested on a set of 336 real retinal images and evaluated subjectively as there is no golden standard available; it proved the ability of eliminating the illumination

inhomogeneity substantially in most cases, as visible e.g. in Figure 1. The application field of this method, though naturally particularly suitable in preprocessing of retinal images, may be wider in preparation of generic image data for fusion or other higher level processing.

Another often met problem is a low signal to noise ratio (SNR) in measured data that in case of repetitive data (e.g. multiple scans) can be in principle improved by averaging that may be considered a primitive fusion. This kind of preprocessing requires total coherence among repetitions, which cannot be guaranteed in retinal imaging due to eye movements between individual images and, in case of scanning imaging as with scanning laser tomography (SLT), even during individual scans, so that the scan lines become mutually shifted. To prevent these inconsistencies, the images must be flexibly registered taking into account the characteristic types of distortions ahead of averaging; this particular problem has been treated in [41] and [42]. As the method belongs to the more generic area of retinal image registration, it will be treated in section 2.2. An example of averaging without and after registration, aimed at SNR improvement for detection of autofluorescence (AF) areas, is shown in Figure 2. The quality improvement thanks to the preliminary registration is obvious. In a series of cases, the average gain in SNR for averages of available groups of nine images was approximately 4dB, which corresponds well to the theoretical value 4,77dB.

Wide spectrum of preprocessing methods has been used to arrive at the referred to results, however only those with a methodological novelty were treated here in a degree of detail. However, it should be mentioned that the way of using the standard methods, like convolutional or non-linear operators for parametric image derivation or edge enhancement, Perona-Malik's anisotropic diffusion [62] or median filtering for edge preserving smoothing etc., has not been always straightforward; a part of the research always aims also at choosing the suitable preprocessing for a particular type of images and adjusting it correspondingly by finding proper details or parameters, as reported in the publications on individual problems.

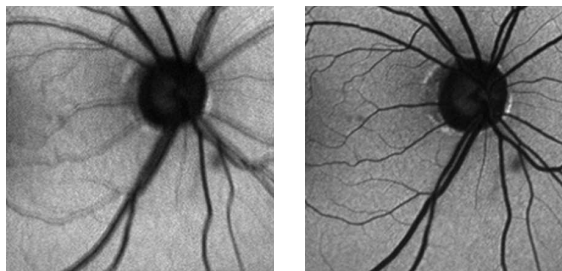


**Fig. 2.** Comparison of averaged AF retina image without preliminary registration and after the described flexible registration. Notice the level of detail and namely the better detectability of the autofluorescence areas

## 2.2. Retinal image registration

The registration of retinal images, as a preparatory step for fusion required for diagnostic purposes [6, 14, 54], iteB6, has certain particularities specific to individual applications that must be taken into account when designing the registration methods for particular purposes, as in [33, 37, 41, 42]. All the registration methods [52, 72] have a common approach – searching for a geometric transform  $T(\boldsymbol{\alpha})$  that best describes the spatial relationship between the details in the reference image and the corresponding details of the registered image. The concrete shape of the transform is determined by its parameter vector  $\boldsymbol{\alpha}$ , the optimal value of which is found by the optimisation

$$\boldsymbol{\alpha}_0 = \arg \left\{ \min_{\boldsymbol{\alpha}} C(R(x), F(T_{\boldsymbol{\alpha}}(x))) \right\}, \quad (7)$$

where  $R(\mathbf{x})$  is the reference image and  $F(T_{\boldsymbol{\alpha}}(x))$  is the floating image to be registered to  $R(\mathbf{x})$  by the spatial transform  $T(\boldsymbol{\alpha})$ . Registration quality, corresponding to the transform  $T_{\boldsymbol{\alpha}} = T(\boldsymbol{\alpha})$ , is evaluated by a chosen similarity criterion  $C$ .  $T(\boldsymbol{\alpha}_0)$  is then the optimal registering transform with respect to the criterion. The choice of  $C$ , of type of the transform  $T$ , of the interpolation method used to find values of  $T_{\boldsymbol{\alpha}}(F)$  on the pixel (voxel) grid of  $R$ , and of the optimisation algorithm to determine the optimal  $\boldsymbol{\alpha}_0$  is crucial for successful registration of a particular type of images.

The registration problems solved in the DAR frame were both monomodal and multimodal. In a series of papers [6, 37, 38, 39, 57, 65], gradual development of bimodal registration method of fundus camera images with the 2D projections of SLT image data is described. As the similarity criterion  $C$ , the mutual information  $MI(\dots)$  is in principle used, as described e. g. in [25],

$$MI(R, T_{\boldsymbol{\alpha}}(F)) = H(R) + H(T_{\boldsymbol{\alpha}}(F)) - H(R, T_{\boldsymbol{\alpha}}(F)) \quad (8)$$

where  $H(\dots)$  are marginal entropies of individual images,  $T_{\boldsymbol{\alpha}}(F)$  is a short for  $F(T_{\boldsymbol{\alpha}}(\mathbf{x}))$  and  $H(R, T_{\boldsymbol{\alpha}}(F))$  denotes the joint entropy; all entropies are derived from the joint histogram. However, this common criterion turned out having too expressed side extremes, often even false global extremes. Therefore, modified criterion has been suggested,

$$C(R, T_{\boldsymbol{\alpha}}(F)) = MI(R, T_{\boldsymbol{\alpha}}(F)) \cdot GI(R, T_{\boldsymbol{\alpha}}(F)) \quad (9)$$

where  $GI(\dots)$  is mutual information among the respective gradient images,

$$GI(R, T_{\boldsymbol{\alpha}}(F)) = H(|\nabla R|) + H(|\nabla T_{\boldsymbol{\alpha}}(F)|) - H(|\nabla R|, |\nabla T_{\boldsymbol{\alpha}}(F)|).$$

The criterion (9) proved very efficient for the given types of images.

The choice for type of  $T$  in this case was the affine transform that proved to allow sufficiently precise registration, as statistically confirmed by extensive testing and represented in an example in Figure 3. This result together with a high reliability of a proper registration was also conditioned by a suitable choice of the interpolation method and of optimisation algorithm correspondingly treating the complexity of the

shape of the similarity criterion function. Among the tested optimisation algorithms, two proved efficient – simulated annealing and controlled random search (CRS); the latter was then found the most reliable under different circumstances. Therefore, the CRS algorithm [68] has been used for optimisation in most of the registration work described in this paper; only for final tuning of the transform parameter, i. e. in the close neighbourhood of the optimum, more efficient Nealder–Mead method could be used relying on local quadratic approximation of the criterion function.



**Fig. 3.** Example of to be registered retina images: left – colour fundus camera image, middle – SLT 2D projection, right – result of the described registration method (edges of fundus camera image overlaid on the SLT image).

In order to achieve high registration reliability, a multiresolution (pyramidal) approach was used. The first pyramid layer is used for finding the optimal scale and translational parameters using four-times subsampled images, while rough detection of the optic disc position helps to initiate the search algorithm. Second pyramid layer using results of the previous step determines the parameters of the used affine transform still in four-times subsampled images; the used optimization approach was the Controlled Random Search (CRS) algorithm [67]. In the third pyramid layer, the parameters are refined by Nealder–Mead method utilising full resolution image data. With this approach a high success rate was achieved – 96,5 % of quality images properly registered according to the statistical tests on clinical material.

Already mentioned preregistration of AF retinal images before averaging [34, 42] used in principle the same approach based on eq. (7); however with some differences crucial for successful registration of the SLT sequences [41]. The retinal images, strongly corrupted by noise, non-homogeneous illumination and motion artefacts, were acquired using a confocal scanning laser ophthalmoscope (Heidelberg Retina Angiograph) in Fluorescein Angiography (FA) mode; a nine-image sequence was taken for each patient to enable averaging. Although the registration problem is monomodal, the variances in imaging conditions (namely illumination and its unevenness) preclude using standard monomodal similarity criteria like sum of absolute or squared differences, or correlation based criteria. The only useful choice proved to be the mutual information as the similarity metrics, however modified by two regularization terms:

$$C(F, T_\alpha(M)) = MI(F, T_\alpha(M)) + w_{comp}E_{comp} + w_{smooth}E_{smooth}, \quad (10)$$

where  $E_{comp}$  is a term penalizing local compression or expansion of the image, derived by summing determinant measures of local Jacobian of the transform  $T(\dots)$  and  $E_{smooth}$  is a constraint term promoting smoothness, i. e. penalizing increase in noise, based on integral of squared second derivative terms over the image support;  $w$  are the respective weights to be determined experimentally.

The transformation compensating distortions due to eye movements during the acquisition of HRA image sequence can be, in our model of geometric distortion, separated into global and local motion components as follows:

$$T(\dots) = T_{global}(\dots) + T_{local}(\dots), \quad (11)$$

where the first component reflects the global eye motion between subsequent scans while the second one the movement of the patient's eye within a single HRA scan (a part of the scan is shifted with respect to other part(s)). The global part has been sufficiently modelled by linear affine transform  $g(\dots)$  with 6 degrees of freedom,

$$g_{global}(x_1, x_2, x_3) = \begin{bmatrix} x'_1 \\ x'_2 \\ w \end{bmatrix} = \begin{bmatrix} a_{11} & a_{12} & a_{13} \\ a_{21} & a_{22} & a_{23} \\ a_{31} & a_{32} & a_{33} \end{bmatrix} \cdot \begin{bmatrix} x_1 \\ x_2 \\ 1 \end{bmatrix},$$

( $a_{31} = a_{32} = 0, a_{33} = 1$ ), while the detailed local deformations are then modelled by free-form deformation (FFD) based on B-splines,

$$T_{local}(\mathbf{X}) = \mathbf{x} + \sum_k \Phi_k \beta^{(n)} \left( \frac{\mathbf{x}}{h} - k \right),$$

where  $h$  is knot spacing,  $n$  is B-spline order and  $\mathbf{k} = [k]$  is index vector of a control point;  $\Phi$  denotes the of control points separated by  $h$ . The number of parameters to be determined in the final phase of registration depends on the grid density and may reach up to 1922. Correspondingly, the registration process is formulated in pyramidal way with gradually increasing resolution: starting with low  $128 \times 128$  resolution, the rough translation is found, as the initiation for optimisation of affine transform by CRS algorithm. Next, in the close vicinity of the optimum, the global transform parameters are refined by Powell's method. In these steps, no regularisation of the  $C$  criterion was needed ( $w_{com} = w_{smooth} = 0$ ). In the second phase, the FFD registration is performed with  $256 \times 256$  resolution, with the density of controlling points gradually increasing from  $11 \times 11$  to  $31 \times 31$ , which provides highly flexible possibilities of coping with complex distortion due to fast eye movement. An intermediate result of the grid deformation is shown in Figure 4.

The corresponding example of the resulting fused (averaged) image without and with the registration is in Figure 2, clearly demonstrating the necessity of precise registration.

Quite different approach to registration [29] has been recently – for the sake of simplicity and speed – applied to another ophthalmological application, requiring to register monomodal images. It combines essentially two approaches: phase correlation for preliminary registration by the rigid transform (determining both shift

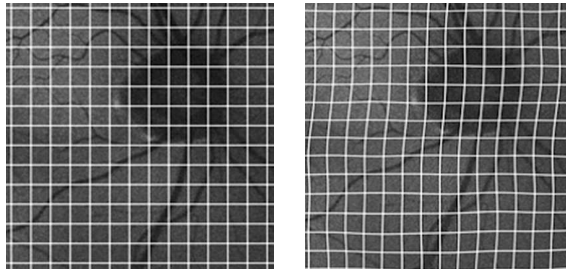


**Fig. 4.** Example of the controlling grid on a to be registered image before and after the flexible registration transform specific for the particular image.

and rotation), and the landmark correspondence based approach that provides sufficient number of linear equations to determine parameters of the refining quadratic transform.

A similar problem to registration is the disparity analysis in a couple of fundus camera images provided with different aspects that serve for stereo based reconstruction of the surface of the OD area [31].

### 2.3. Segmentation in retinal images

Automatic segmentation of medically important areas and objects in retinal images is of prime importance for support of diagnosis of many serious diseases, particularly, when screening methods are considered. Therefore much effort is generally devoted to this area. On the other hand, the reliability of the segmentation, as the shape, size, position and orientation etc. of the segmented objects concerns, is often vital for the diagnosis and very high reliability is thus required, mostly not achievable so far with contemporary fully automatic methods, although the symptomatic features on the retinal appearance or image may be well recognised by experienced ophthalmologist. That is why some of the approaches are still only semi-automatic leaving the difficult decisions, concerning either the medical conclusions based on the segmentation or the often vital initialisation of otherwise automatic algorithms, on a medical expert. Definitely, the final results of even fully automatic procedures must be always medically approved. Several directions of segmentation have been treated in our group: the “classical” problem of optical disc (terminal of the optic nerve bundle) segmentation, segmentation of the vessel tree in the fundus camera images, alternative approach of segmenting the vessels from optical coherence tomography (OCT) data, and particular disease indicating regions, as autofluorescent (AF) areas.

#### 2.3.1. Optical disc segmentation

Segmenting the optical disc (OD) is a principal task in retinal image analysis and some related work has been published previously [7, 14, 65]; the subject of our reported research were the algorithms improving the segmentation by a kind of fusion of fundus camera images and LST data. Papers [6, 57], published in cooperation

with the Erlangen group summarize the achieved level before the DAR centre started. These methods utilised bimodal imaging – fundus camera and LST images in which the segmentation was done individually after registration of both images. This OD segmentation method by Chrastek was based on a specialised type of flexible contours, controlled by so called anchors respecting the prior anatomical knowledge; the contours were initiated by applying Hough transform on edge representation of each of the fused images. The fusion was then done at the level of results of individual OD segmentations with obvious improvement in reliability and precision compared to segmentation from only single modality. Newer contribution [37] tries to improve the segmentation further by first fusing both images registered by procedures described in section 2.1.2 while the segmentation is performed subsequently in the derived scalar image. The conversion of the fused vector-valued image to the corresponding scalar-valued one is made as in [64] using a formal 2D dyadic wavelet transform applied to both images. The obtained discrete wavelet spectra are coefficient-wise combined based on strictly formal rules thus providing the fused spectrum, which is then converted back to the original domain, yielding a scalar-valued image. The resulting image is expected to carry the decisive information, which should enable well defined and hopefully better segmentation.

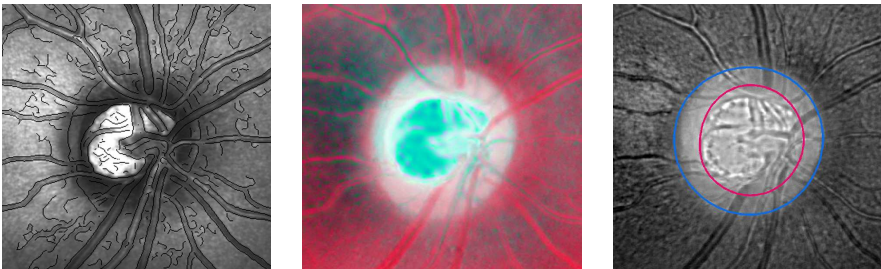


**Fig. 5.** (from left) – SLT image with superimposed edges from fundus camera image, fused colour fundus camera image (each colour band is fused with SLT image), scalar fused image (three bands of fundus camera image and SLT image are fused into a scalar image) with segmented inner and outer optic nerve head contours.

An example of using this approach is in Figure 5, showing the registered images, colour representation of partially (by colour bands) fused fundus image with the SLT image and finally the fused scalar image with the segmented inner and outer contours of the optical disc. The segmentation has been done by the modified Chrastek’s method [6].

### 2.3.2. Vessel tree segmentation

A classical problem is segmentation of vessel tree on retinal images, needed primarily for diagnosing diseases that are manifested by characteristic changes, namely diabetes, and newly also for personal identification.

This area has been covered by many publications, as e.g. [5, 9, 15, 28, 44, 58, 59, 70]; our results [26, 60] are bringing a novel approach based on 2D matched

filtering. The analysed material is formed by high resolution fundus camera images of  $3504 \times 2336$  pixels, enabling to follow intensity profiles of even thin vessels. Although the input to the procedure is a single image, the method utilises fusion concept when nonlinearly combining derived parametric images. This approach is based on multiple use of 2D directional matched filtering locally evaluating occurrence of vessel segments of a particular width and orientation. The filter masks have been derived based on measured and averaged brightness profiles of vessel segments of five different width classes, from narrow to wide. The masks for the 2D matched filtering were then designed by plain parallel back-projection of the averaged profiles  $p_i(\tau)$  over the 2D masks  $M_i(x, y)$ ,

$$M_{i,j}(x, y) = p_i(\tau(x, y, \varphi_j)) = p_i(x \cos \varphi_j + y \sin \varphi_j)$$

in 12 directions, thus providing the corresponding mask matrices  $\mathbf{M}_{i,j}, i \in \langle 0, 4 \rangle, j \in \langle 0, 11 \rangle$ .

Every averaged profile generates 12 differently oriented masks – i. e. discrete point spread functions (PSFs) of the filters (Figure 6).

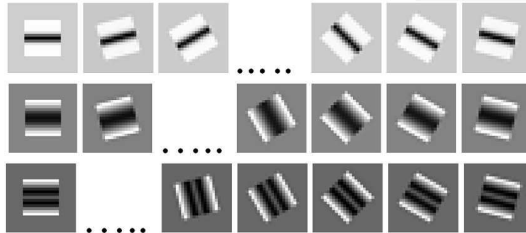


**Fig. 6.** Examples of masks of the matched filters for narrow (top) to wide (bottom).

By convolving  $I(x, y)$  with each of the masks  $M_{i,j}(x, y)$ , in matrix notation

$$\mathbf{P}_{i,j} = \mathbf{M}_{i,j} * \mathbf{I}, \tag{12}$$

60 parametric images  $\mathbf{P}_{i,j}$  are obtained that individually quantify the local presence of the respective vessel section for each pixel in the input image  $\mathbf{I}$ .

Results of the filtering – the respective 2D parametric images – are then processed and combined first into the rough description of the vessel structure including the width and orientation information, as follows. Twelve parametric images  $\mathbf{P}_{i,j}$  for a particular width range  $i$  are then pixel-wise fused into the intensity image  $\mathbf{R}_i$

$$\mathbf{R}_i(k, l) = \max_j \mathbf{P}_{i,j}(k, l), \quad \forall k, l,$$

discarding the orientation information. This way, five fused parametric images  $\mathbf{R}_i$  for individual vessel width ranges  $i$  are obtained. Each of the images  $\mathbf{R}_i$  is then individually thresholded using an adaptive threshold determined by maximization of local entropy. This way, five binary images indicating primarily the locations of vessels of  $i$ th width range, are provided. Finally, the rough binary vessel image  $\mathbf{S}$  is fused as

$$\mathbf{S}(k, l) = \bigcup_i \mathbf{R}_i(k, l). \tag{13}$$

Individual vessel pixels in  $\mathbf{S}$  may be additionally labelled according to the maximum-response width range,

$$\mathbf{W}(k, l) = \arg \max_i \mathbf{R}_{i,j}(k, l),$$

by which the rough vessel map  $\mathbf{W}$  is provided carrying the width information. An example is shown in Figure 7 (left – colour code from red through to blue for  $i = 0, \dots, 4$ ); in the detail the wider segment traces are composed typically of central line indicating the segment width surrounded by responses to vessel walls as narrow structures but the total width of the vessel is well represented by the resulting trace.

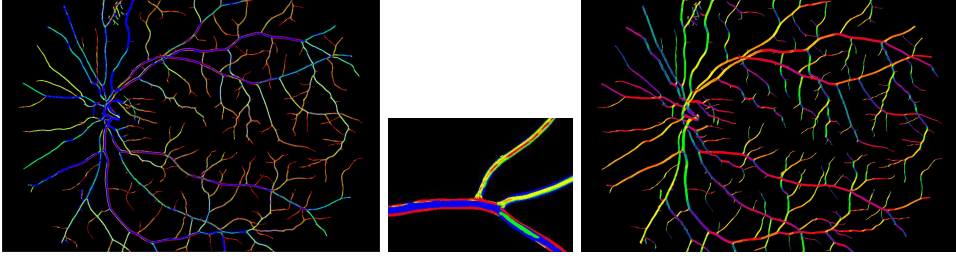


**Fig. 7.** (from left) Rough width map  $\mathbf{W}$  of the vessel tree, a detail showing the local width representation, corresponding directional map.

The directional map  $\mathbf{D}$  (Figure 7 right) indicating the local vessel orientation can be derived as

$$\mathbf{D}(k, l) = \arg \max_j (\nabla_i \mathbf{P}_{i,j}(k, l)).$$

The width and orientation maps  $\mathbf{W}$  and  $\mathbf{D}$  can be used for a consistence check of the resulting vessel tree and for the following connectivity improvement of the rough binary vessel tree  $\mathbf{S}$ . This is done by a set of heuristics improving connectivity in  $\mathbf{S}$  by complementing the obviously missing short sections of continuous vessels and cleaning disconnected elements appearing due to noise, thus providing the final binary vessel tree image (Figure 8).

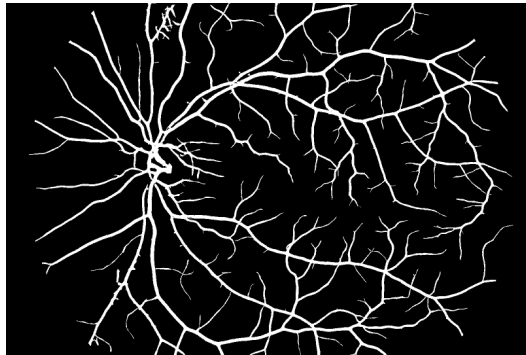


**Fig. 8.** Resulting vessel tree map.

The efficiency of the segmentation method has been primarily evaluated using the international database DRIVE of retinal images segmented manually by medical experts. In this test, our method, though working satisfactorily for thick and medium vessels, omits some of the thinnest ones due to low resolution of the database images as the 2D matched filtering cannot detect the vessels of single-pixel or sub-pixel width that nevertheless can often be detected visually by an expert. However, with the higher resolution clinical images, the automatically derived results are well comparable with what can be discovered visually, including the narrowest vessels; by comparison with published results (though on different images) it may be concluded that no better automatic segmentation approach is available. The designed method thus represents one of important results.

Different vessel tree segmentation or rather reconstruction approach [16] aims at localizing individual OCT scan-lines (B-scans, Figure 9) in the corresponding fundus camera image. It utilises fusion of individual B-scans of the 2D OCT scan structure provided by scanning the retina along parallel lines thus providing coverage of a rectangular image area. In the B-scans, the vessels cause vertical shadows that can be utilised for detection of the vessel positions and widths on the scan line. However, the individual scans are mostly deformed and have to be geometrically rectified before the position of the vessels can be determined. To this end, the lowest layer of the B-scan profiles, retinal pigment epithelium (RPE) must be identified via a gradient technique and segmented as a curve to be straitened in the individual scans; consecutively, the image is rectified by a polynomial transform. Finally, the individual vessel positions are located along the parallel lines of the 2D image, as in Figure 10. Registering the reconstructed OCT vessel image with the retinal image is the way to localisation of the OCT scan lines in the fundus camera image, which enables comparison of rough retinal neural layer detection on fundus camera image with the objective measurement provided by OCT.

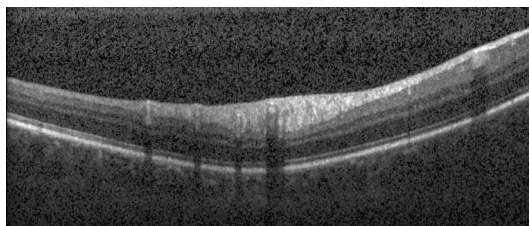


**Fig. 9.** Single B-scan (cross-sectional depth map) of a retina along a line.

### 2.3.3. Autofluorescence areas segmentation

A rather special type of retinal image examination concerns the autofluorescent (AF) zones formed by lipofuscin granules in the retinal pigment epithelium in the parapapillary region near to the optical disc, which have been found diagnostically important particularly for open angle glaucoma and ocular hypertension [4, 11, 43, 47, 50, 69]. They can be imaged and AF level and distribution thus estimated by the SLT equipment working in a special mode, using a low-pass filter for detection of emitted light



**Fig. 10.** Fused blood-vessel image based on OCT scans (left), the corresponding fundus camera image.

above  $\lambda = 500$  nm, after the autofluorescence was excited by illumination with blue argon laser ( $\lambda = 488$  nm). The image analysis required so far manual outlining of the AF areas; this is not only time-consuming but the results of manual segmentation suffer generally with a high inter-observer variability. The aim of the AF project described in [30, 35], and [36] was therefore to develop a semi-automatic segmentation method that would both save the medical expert effort and also limit the variance.

The analysis of the SLT AF images starts with localisation and segmentation of OD, in the neighbourhood of which the AF areas with a higher accumulation of lipofuscin may appear as small brighter isles; however, their contrast may be rather low. In order to simplify the algorithm and to increase the reliability of the segmentation, the seeds of the AF areas are pointed to by the medical expert; the rest of the segmentation is automatic. The procedure is based on region growing method starting from the seeds, the localisation of which is automatically refined by inspecting  $5 \times 5$  neighbourhood of the original seed and choosing the highest intensity pixel, in order to diminish the precision requirements to the user. The region growing is dynamically controlled by the varying mean  $m_R$  of the growing area: a candidate pixel  $p_c$  is only added to the area R when

$$\text{abs}(m_R - p_c) < T,$$

where  $T$  is a chosen threshold to be found experimentally. The final results are naturally sensitive to this parameter that may influence not only the important size but also merging of neighbouring areas whose number is diagnostically important as well. As an additional operation, the obtained AF areas are automatically evaluated for their position with respect to OD, their shape and size.

Statistical evaluation of the reliability and consistence of the method has been performed on a relatively large clinical image set of 20 glaucomatous patients. In the lack of standard segmentation methodology for AF areas, automatically determined AF areas in several AF zones were compared with the expert manual segmentation. Large differences among manually segmented areas could have been observed, while generally a reasonable agreement of the described method with averaged expert results was found. Images presented in Figure 11 show the results of both the automatic and manual segmentations (by three different experienced ophthalmologists).

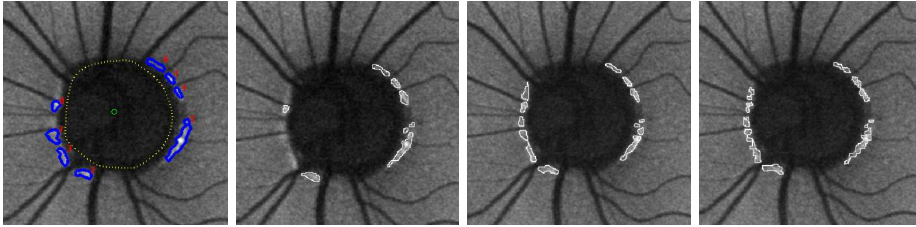


**Fig. 11.** (From left): Example result of semiautomatic segmentation, and three independent results of manual segmentations by three experienced ophthalmologists.

A high inter-operator variability is visible; in this frame the automatic results are generally well comparable. The analysis demonstrates utility of the semiautomatic segmentation method that suppresses the variability.

#### 2.4. Feature extraction and classification of NFL

Retinal neural fibre layer (NFL) status is an important indicator of some serious diseases, particularly of glaucoma, which is a relatively frequent cause of sight damage or loss [1, 3, 8, 12, 19, 27, 51]. This is caused by deterioration of retinal neural fibre layer (NFL) that provides connection between the light sensing elements of eye and the sight nerve bundle leaving the retina at the optical disc. The degree of NFL damage is an indicator of the disease progression, which can be hindered or even stopped if discovered early; that is why automatic screening methods for generic use (easy and cheap) are required by the ophthalmologic community. Ophthalmologists can assess the NFL status visually, evaluating standard fundus camera retinal images (Figure 3 left), where NFL shows up as a very faint stripy structure, usually lighter than regions with defective or lacking NFL. Local brightness is the main feature used in visual evaluation; however this is unreliable due to spatially varying illumination of retina; the evaluation thus requires great experience and the subjective results suffer with a large interpersonal variance. The OCT, which measures local thickness of NFL structure quantitatively, is presently considered the best among the automatic NFL evaluating methods; however, it is still rather expensive and demanding to be used for screening. To this purpose, fundus camera thus remains the most commonly available data source with a good potential for basic NFL screening, if suitable objective analytic methods are provided, although practically only rough classification into healthy and missing NFL is possible. Even though several attempts from different aspects have been previously published [18, 44, 45, 55, 58], the problem is still open and topical.

Our approach to detecting healthy / missing NFL areas in retina images (see the detail in Figure 12) is based on evaluating and classifying a number of differently defined local features in fundus camera images potentially characterising the NFL. As these textural characteristics are individually barely visible and their evaluation is therefore of low reliability, multiple features forming a feature vector have to be submitted to classification algorithms, enabling then to achieve a reasonably reliable NFL detection. As the texture analysis would be heavily disturbed by the structure

of retinal vessels, this must be detected and segmented out before the NFL analysis; a highly reliable segmentation of the vessel structure (section 2.1.3) is thus a crucially important step in the FNL analysis.

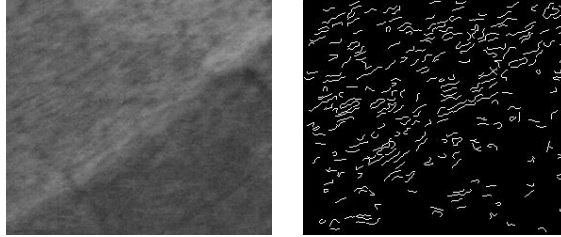


**Fig. 12.** From left: Detail of retina image showing the stripy appearance of NFL area in its upper left half and the corresponding modified edge map after cleaning.

## 2.5. Texture analysis of NFL

In [26] and [20], a complex method to detect the presence of NFL is described, using three textural approaches that proved relevant, each providing a vector-valued feature image quantifying the NFL presence according to particular criteria. Subsequently, four chosen local features derived from these partial results form a local feature vector submitted to a learning classifier, which provides the local NFL assessment. The evaluation is provided for node pixels of a square grid  $4 \times 4$  over the image  $\mathbf{U}$  with  $\mathbf{x}_k$  being the position of  $k$ th node point. The local square-shaped  $N \times N$  blocks  ${}_k\mathbf{X}$  used for determining the node textural parameters are centred around  $\mathbf{x}_k$ ;  $N$  is generally different for each of the used analytic approaches, described below.

*Directional spectral analysis* – the most relevant approach – aims at detecting the faint stripy appearance of the neural layer (as in Figure 12 left) due to locally parallel fibre orientation, which may be detectable in local spectra of small NFL areas ( $N = 128$ ), into which the analysed image is subdivided. The spectral analysis is performed for every local block  ${}_k\mathbf{X}$  by 2D-DFT transform after weighting with 2D Tukey circular window ensuring that the operator is isotropic. Each of the obtained local amplitude spectra (Figure 13) is subdivided into overlapping angular sectors  $s_l$ , and the sector spectral energies  $P$  are calculated as

$${}_k^l P = \sum_u \sum_v |{}_k^l F_{u,v}|^2, \quad u, v \in s_l, \quad l = 1, 2, \dots, 22,$$

where  $u, v$ , are spatial frequency indices and  $F$  are the spectral coefficients. Two features may be derived from these directional spectral energies: the local NFL intensity assessed by the degree of non-isotropy characterised by the difference in extreme directional energies,

$$F_1(\mathbf{x}_k) = \max_l ({}_k^l P) - \min_l ({}_k^l P),$$

and the local NFL orientation given by the index of the maximum energy sector,

$$F_2(\mathbf{x}_k) = \arg \max_l ({}_k^l P),$$

which, however, would contribute to the efficiency of the classification only when the local orientation could be compared to a standard directional map, which is not yet available.

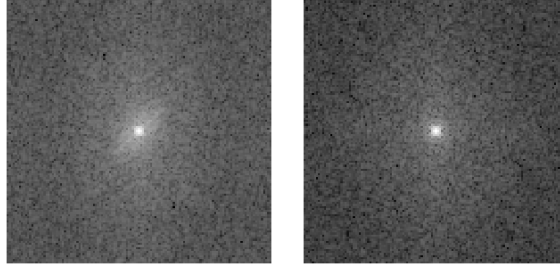


**Fig. 13.** Local amplitude spectra of areas with NFL detected (left) and missing (right).

*Edge based approach* derives the features from the binary edge map  $\mathbf{I}_{edge}$  obtained by convolution of the retinal image with Laplacian of Gaussian operator ( $N=13$ ) followed by non-linear zero-crossing detection. Two features are then derived from the map after cleaning small objects (Figure 12 right):

the percentage of edge pixels in the block ( $N=129$ ),

$$F_3(\mathbf{x}_k) = \sum_i \sum_j I_{edge}(i, j) / N^2,$$

and the mean of lengths of the edge segments  $l_{edge}$ ,

$$F_4(\mathbf{x}_k) = \frac{1}{2M} \sum_{m=1}^M l_{edge}(m).$$

Although edges are detected with low reliability due to faintness, they proved to provide useful information this way. A feature, describing the prevailing local direction of the FNL edges, has not been derived as its utility is low due to lack of a standard directional map.

*Brightness based feature* has been introduced as mimicking the approach primarily utilised by medical experts for NFL classification, although it is obvious that it might be only an auxiliary criterion due to uneven illumination in retinal images. It utilises the fact that areas with missing neurons are on average slightly darker than healthy areas; a simple feature comparing the locally smoothed brightness at the node  $\mathbf{x}_k$  with the average brightness of the total region of interest (ROI) is

$$F_5(\mathbf{x}_k) = \sum_{i,j \in ROI} I'_{i,j} - \sum_{i,j \in_k \mathbf{X}} I'_{i,j}.$$

As the NFL detection is computationally rather demanding, a smaller region of interest (ROI) is automatically determined in a retinal image, encompassing the diagnostically important area around optical disc extended towards macula, as in

Figure 14; this naturally requires preceding optical disc segmentation (section 2.1.3). The local NFL status is classified in the ROI based on the local feature vector

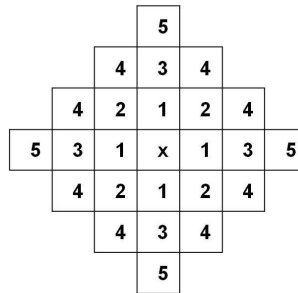
$$\mathbf{F}(\mathbf{x}_k) = [F_1(\mathbf{x}_k), F_3(\mathbf{x}_k), F_4(\mathbf{x}_k), F_5(\mathbf{x}_k)]. \tag{14}$$

The features were selected based on experimental verification of their relevance with respect to separability of both classes considering the means and variances. Further on, the relevance of individual features was confirmed by comparing the classification results with each of the features individually omitted from the vector; in all cases, the success rate increased when a feature was added.

Another our textural approach to NFL detection is [61], where the texture is modelled by Gaussian Markov random fields (GMRF), the parameters of which serve then as classification features to recognize healthy and diseased NFL in retinal fundus images. The modelling, based on Markov random field modelling theory [46], is describing probability of spatial interactions in a textural image and has been used in many image processing applications, e. g. [63]. In our application, the GMRF is modelling the image texture  $y(\mathbf{x})$ , which is considered a set of zero mean observations  $y(\mathbf{x}), x \in \Omega$  for an  $M \times M$  image lattice  $\Omega$ . The GMRF model is a 2D stationary non-causal autoregressive process where the individual observations are generated by the difference equation

$$y(\mathbf{x}) = \sum_{\mathbf{r} \in N_{\mathbf{r}}} \phi(\mathbf{r})y(\mathbf{x} + \mathbf{r}) + e(\mathbf{x}); \tag{15}$$

here  $N_{\mathbf{r}}$  is a chosen neighbourhood set centred at pixel  $\mathbf{x}$ ,  $\phi(\mathbf{r})$  is the model parameter belonging to the neighbour located at radius  $\mathbf{r}$ , and  $e(\mathbf{x})$  is a stationary Gaussian noise process with zero mean and a known variance  $\sigma^2$ . Fifth-order circularly symmetric neighbourhood has been shaped on rectangular lattice as where the numbers



indicate the indices of the five different parameters  $\phi(\mathbf{r})$ . The GMRF model thus has 6 parameters – textural features: 5 weight parameters describing the influence of the neighbours to the central pixel plus the noise variance  $\sigma^2$ . These 6 features

can be estimated in the least square error sense via the following equations:

$$\phi(\mathbf{r}) = \left[ \sum_{\Omega} q(\mathbf{x})q^T(\mathbf{x}) \right]^{-1} \left( \sum_{\Omega} q(\mathbf{x})y(\mathbf{x}) \right),$$

$$\sigma^2 = \frac{1}{M^2} \sum_{\Omega} (y(\mathbf{x}) - \phi^T q(\mathbf{x}))^2,$$

where

$$q(\mathbf{x}) = \text{col} \left[ \sum_{r \in N_i} y(\mathbf{x} + \mathbf{r}); i = 1, \dots, 5 \right].$$

The features then form the local vector to be used in the NFL classification,

$$\Phi(\mathbf{x}) = [\phi_1(\mathbf{x}), \phi_2(\mathbf{x}), \phi_3(\mathbf{x}), \phi_4(\mathbf{x}), \phi_5(\mathbf{x}), \sigma^2(\mathbf{x})]. \quad (16)$$

Although this approach provided well acceptable results, more elaborate models (e. g. with expressed anisotropy) are considered as candidates for future research. This might better reflect the existing anisotropy of the NFL.

Presently, still other textural features are under investigation in partial projects, e. g. based on run-length or co-occurrence matrices. Another such attempt is in [32], using fractal model of the NFL texture; the fractal dimensions are used as relevant features. Generally, the tendency is to provide a higher number of possibly only weakly relevant features that however may lead to increasing the efficiency of the NFL classification from fundus camera images.

### 2.5.1. NFL classification

Of the different types of classifiers tested in frame of the retinal project, several have shown a sufficient and essentially comparable efficiency – feed-forward layered neuronal networks (NN) (e. g. in [20]), vector support machines (in [32]) and Bayesian classifiers (in [61]). Of them, particularly two ones are mentioned here in a degree of detail concerning also the classified material. In [20], a simple feed-forward layered neural network with error back-propagation learning provided the best results. Its learning was based on a selection of blocks from the available image material, while the testing utilised a disjunctive similarly chosen block set. The available material concerned ten patients; out of them, seven patients suffered with a degree of NFL deterioration, while the remaining three were healthy. Altogether 564 blocks sized  $129 \times 129$  pixels were obtained from the above defined ROIs, out of which 164 were indicated by medical experts as lacking the FNL, while the remaining 400 blocks were considered healthy. In the lack of any golden standard, testing of the classification based on feature vectors (14) was only possible in comparison with the visual evaluation of images by experienced medical experts.

The achieved success rate of the classification in the test set was 93,36% that can be considered a very good result when considering the high interpersonal variance of the medical decisions in this area. The results may be presented as segmentation of areas with presence or absence of the NFL at the node pixels of the above mentioned

grid in the ROI, i. e. as an overlay on the retinal image with greenish areas for healthy and reddish for the areas lacking NFL, as in Figure 14, where also medical-expert NFL diagnoses are indicated (though a little uncertain ones). There is quite a good agreement generally between the automatic and manual classification; in some cases, when the NFL is very faint, the automatic detection seems to recognise the NFL even when it is not detected visually.

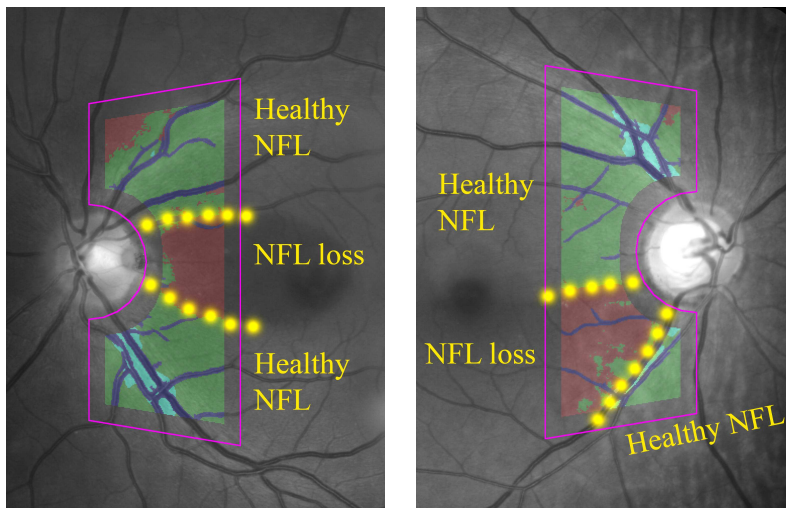


**Fig. 14.** Examples of automatic NFL detection in fundus camera images (ROI represented by violet frames, greenish/red overlay – healthy/ lacking NFL) compared to areas estimated by medical experts (white dotted borders).

As the first step towards objective evaluation of the fundus camera image classification based on feature vectors (14), a comparison has been made of its results with the objective measurements of the NFL thickness by the OCT method. In total 92 image areas medically evaluated areas (42 lacking NFL, 50 healthy) were mutually registered in both modalities. These tests have shown obvious correlation between the medical decision, the used features and objectively measured thickness of the NFL. An example showing the OCT B-scan and the corresponding evaluated fundus camera image with indicated line of the scan is shown in Figure 15.

In [61], a Bayesian classifier, expecting Gaussian probability distribution of individual classes in the feature space, determining the class by maximizing the probability of individual classes conditioned by a particular feature vector  $F$ ,

$$k = \arg \max_k P(\omega_k | \mathbf{F}), \quad P(\omega_k | \mathbf{F}) = \frac{p(\mathbf{F} | \omega_k) P(\omega_k)}{p(\mathbf{F})}, \quad (17)$$

has been used for classification of the experimental image material. The probability distribution of a class  $p(\mathbf{F} | \omega_k)$  as well as the prior class probability  $P(\omega_k)$  is determined during training the classifier using the training data set, while  $p(\mathbf{F})$  is just a scaling factor. The extensive experiments based on the feature vector (16) proved

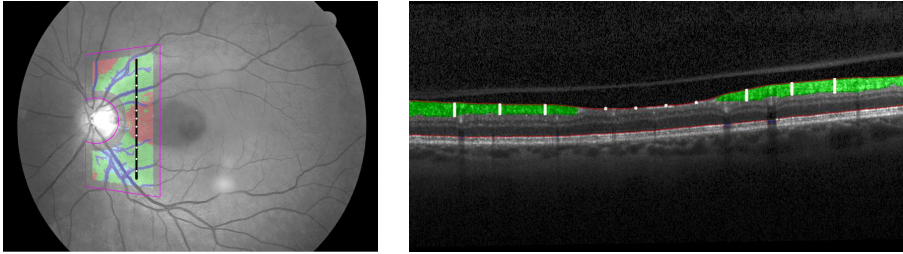


**Fig. 15.** Comparison of NFL detection in a fundus camera image (left) and OCT scan along the indicated trace (NFL is green marked).

the discrimination ability of the proposed GMRF features. The iterative maximum-likelihood estimate [13] with optimization technique based on modified expectation maximization algorithm has been used. The GMRF method has been tested on image regions  $97 \times 97$  pixels, manually selected from the available 28 retinal images and classified by a medical-expert. The regions (examples in Figure 16) are divided into three classes: A – regions from glaucomatous eyes still with NFL (intermediate cases), B – regions from glaucomatous eyes with total NFL loss, C – regions from healthy eyes with normal NFL (most pronounced stripy texture).

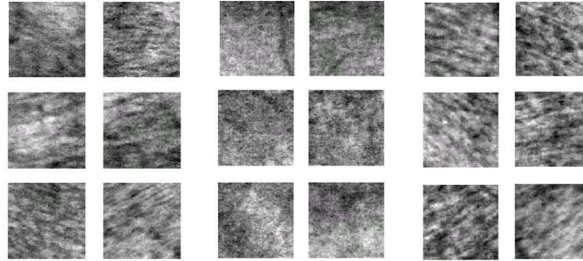


**Fig. 16.** Examples of selected image regions  
(from left to right: class A, class B, class C).

When binary decisions were concerned, naturally best separation was achieved between classes B and C with the lowest error rate under 1%; less pronounced separability has been found with about 3% error rate for A-B combinations. When all three classes are to be resolved, as in Figure 17, the error rate increases to 9.9%, while the worst error rate of 11.7% corresponds to binary case in the least differing groups A and C.

The GMRF results have been also preliminarily compared to OCT measurements with similar positive conclusion as for the previous method. These good results suggest that the GMRF features (16) might complement those included in the vector (14), this way expectedly enhancing the segmentation quality of the NFL areas.



**Fig. 17.** Example of GMRF based classification of NFL ( three classes: green – healthy layer, red – lacking NFL, yellow – intermediate class).

### 3. DISCUSSION AND CONCLUSIONS

As already mentioned, the overview character of the paper encompassing different though connected topics precludes discussing the individual results and conclusions in too concrete detail here; the individual brief discussions were included at respective places in Chapter 2. However, it can be generally stated that the long-term continuous research in the area of ophthalmologic image analysis provides consistent and methodologically novel results that, besides being interesting for the image processing community, are particularly welcome by the cooperating medical colleagues, who implement them partly in their routine or research procedures. Another point is the positive influence of the research centre DAR on the team forming, concentration of people interests to a particular area, and, last but not least, also to the education of young scientists in frame of their doctoral study, when they have this rather exceptional opportunity to participate on such a team effort. It can be concluded, that, together with the presented results, these very positive side effects definitely justify establishing and maintaining the Centre, without which a greater part of the results as well as of the good generic influence would not be accomplished.

### ACKNOWLEDGEMENT

This work has been supported by the DAR – research center no. 1M0572 coordinated by the Institute of Information Theory and Automation of the Academy of Sciences of the Czech Republic, and partly also by the institutional research frame no. MSM 0021630513, both sponsored by the Ministry of Education of the Czech Republic. The authors highly acknowledge the cooperation with the University Eye Clinic in Erlangen–Nurnberg, Germany (G. Michelson, R. Tornow, R. Laemmer, Ch. Mardin), providing us with the image data and evaluating the results from medical point of view, similarly as the Outpatient Eye Clinic of T. Kubena in Zlin, Czech Republic. Also the cooperation with the Pattern Recognition Dept. of the Erlangen University (H.Niemann, J. Hornegger, R. Chrastek and doctoral students) bringing ideas in fruitful discussions, is highly acknowledged.

(Received July 5, 2010)

## REFERENCES

- 
- [1] R. Bock et al.: Glaucoma risk index: automated glaucoma detection from color fundus images. *Medical Image Analysis* 14 (2000), 3, 471–481.
  - [2] B. H. Brinkmann, A. Manduca, and R. A. Robb: Optimised homomorphic unsharp masking for MR greyscale inhomogeneity correction. *IEEE Trans. Med. Imag.* 17 2, 161–171.
  - [3] D. L. Budenz: Reproducibility of retinal nerve fiber thickness measurements using the stratus OCT in normal and glaucomatous eyes. *Invest. Ophthalmology and Visual Science* 46 (2005), 2440–2443.
  - [4] C Bellmann: Topography of fundus autofluorescence with a new confocal scanning laser ophthalmoscope. *Ophthalmology* 94 (1997), 385–91.
  - [5] T. Chanwimaluang and G. Fan: An efficient blood vessel detection algorithm for retinal images using local entropy thresholding. *Proc. Int. Symp. Circuits & Systems'03*, 5 (2003), 21–24.
  - [6] R. Chrástek, H. Niemann, L. Kubečka, J. Jan, V. Derhartunian, and G. Michelson: Optic nerve head segmentation in multimodal retinal images. In: *Proc. SPIE 2005*, Bellingham 2005, pp. 1604–1615.
  - [7] R. Chrástek et al.: Segmentation of the optic nerve head for glaucoma diagnosis. In: *Proc. SPIE 2005*, Bellingham 2005, pp. 1604–1615.
  - [8] T. A. Ciulla, C. D. Regillo, and A. H. Harris: *Retina and Optic Nerve Imaging*. Lippincott Williams and Wilkins, Philadelphia 2003.
  - [9] M. J. Cree, D. Cornforth, and H. F. Jelinek: Vessel segmentation and tracking using a two-dimensional model. *IVC New Zealand* (2005), 345–350.
  - [10] B. M. Dawant, P. Zijdenbos, and R. A. Margolin: Correction of intensity variations in MR images for computer-aided tissue classification. *IEEE Trans. Med. Imag.* 12 (1993), 4, 770–781.
  - [11] F. C. Delori et al.: In vivo fluorescence of the ocular fundus exhibits retinal pigment epithelium lipofuscin characteristics. *Invest. Ophthalmol. Vis. Sci.* 12 (1995), 718–29.
  - [12] P. M. Dodson: *Diabetic Retinopathy*. Oxford University Press 2008.
  - [13] M. A. T. Figueiredo and A. K. Jain: Unsupervised learning of finite mixture models. *IEEE Trans. Pattern Analysis and Machine Intelligence* 24 (2002), 3, 381–396.
  - [14] M. J. Greaney et al.: Comparison of optic nerve imaging methods to distinguish normal eyes from those with glaucoma. *Invest Ophthalmol Vis. Sci.* 43 (2002), 1, 140–145.
  - [15] E. Grisan et al.: A new tracking system for robust extraction of retinal vessel structure. In: *Proc. 26th IEEE EMBC 2004*, San Francisco 2004, pp. 1620–1623.
  - [16] J. Gazárek, R. Kolář, J. Jan, and J. Odstřčilík: Blood vessel tree reconstruction in retinal OCT data. In: *Proc. EURASIP Conf. BIOSIGNAL 2010*, Brno 2010, CD issue, 4 pp.
  - [17] R. Guillemaud and M. Brady: Estimating the bias field of MR images. *IEEE Trans. Med. Imag.* 16 (1997), 3, 238–251.
  - [18] Y. Hayashi et al.: Detection of retinal nerve fiber layer defects in retinal fundus images using Gabor filtering. In: *Proc. of SPIE 6514* (2006).

- [19] St. Hoh: Evaluating the optic nerve head and retinal nerve fibre layer: The role of Heidelberg retina tomography, scanning laser polarimetry and optical coherence tomography. *Annals Academy of Medicine* 16 (2007), 195–202.
- [20] J. Jan, J. Odstrčilík, J. Gazárek, and R. Kolář.: Retinal image analysis aimed at early detection of neural-layer deterioration. Submitted.
- [21] J. Jan, R. Chrástek, and L. Kubečka: Automated optic disc segmentation in multimodal images of retina. In: Proc. DOG/SOE Congress 2005, Berlin 2005, CD issue.
- [22] J. Jan, R. Kolář et al.: Analysis of fused ophthalmologic image data. In: Proc. 6th EURASIP conf. Speech & Image Processing, Multimedia Communications & Services, Maribor 2007, pp. 37–40.
- [23] J. Jan: Retinal image analysis – Brno group). In: SAOT Retina Image Processing Workshop 2009, Erlangen Univ.
- [24] J. Jan: Retinal image analysis aimed at blood vessel structure segmentation and neural layer detection. In: Proc. BEC 2008, Tallin 2008, pp. 31–38
- [25] J. Jan: Medical Image Processing, Reconstruction and Restoration – Concepts and Methods. CRC Press, Taylor and Francis Group 2006.
- [26] J. Jan, J. Odstrčilík, J. Gazárek, and R. Kolář: Retinal image analysis aimed at support of early neural-layer deterioration diagnosis. In: Proc. ITAB 2009, Larnaca, 4 pp., CD issue.
- [27] P. Janknecht and J. Funk: Optic nerve head analyser and Heidelberg retina tomograph: accuracy and reproducibility of topographic measurements in a model eye and in volunteers. *British Journal of Ophthalmology* 78 (1994), 760–768.
- [28] J. Jorge, G. Leandro, M. Roberto et al.: Vessels segmentation in retina: Preliminary assessment of the mathematical morphology and of the wavelet transform techniques. In: XIV Brazilian SIBGRAPI'01 2001, pp. 84–91.
- [29] R. Kolář, V. Šikula, and M. Base: Retinal image registration using phase correlation. In: Proc. 20th EURASIP Conf. BIOSIGNAL 2010, Brno 2010, CD issue, 4 pp.
- [30] R. Kolář, J. Jan, R. Chrástek, R. Laemmer, and Ch. Y. Mardin: Autofluorescence areas detection in HRA images. In: Proc. EMBEC'05, Prague 2005, CD issue.
- [31] R. Kolář, L. Kubečka, J. Jan, and R. Chrastek: Disparity estimation in uncalibrated stereo retina images. In: Proc. EMBEC'05, Prague 2005, CD issue.
- [32] R. Kolář and J. Jan: Detection of glaucomatous eye via color fundus images using fractal dimensions. In: Proc. 6th EURASIP Conf. Speech & Image Processing, Multimedia Communications & Services, Maribor 2007, pp. 37–40.
- [33] R. Kolář, J. Jan, and L. Kubečka: Registration and fusion of the autofluorescent and infrared retinal images. *Internat. J. Biomedical Imaging* (2008), 513478, pp. 1–11.
- [34] R. Kolář, J. Jan, and L. Kubečka: Computer support for early glaucoma diagnosis based on the fused retinal images. *Scripta Medica* (2006), 79, 269–276.
- [35] R. Kolář, J. Jan, and R. Jiřík: Semiautomatic detection and evaluation of autofluorescent areas. In: Proc. IEEE–EMBC 2007, Lyon 2007, pp. 3327–3330.
- [36] R. Kolář, R. Laemmer, J. Jan, and C. Mardin: The segmentation of zones with increased autofluorescence in the junctional zone of parapapillary atrophy. *Physiological Measurement* (2009), 30, 505–516.

- [37] L. Kubečka and J. Jan: Retinal image fusion and registration. In: Proc. EMBEC'05, Prague 2005, CD issue.
- [38] L. Kubečka, M. Skokan, and J. Jan: Optimization methods for registration of multimodal images of retina. In: Proc. IEEE-EMBC, Cancun 2003, pp. 599–601.
- [39] L. Kubečka and J. Jan: Registration of bimodal retinal images – improving modifications. In: Proc. 26th IEEE EMBC, San Francisco 2004, pp. 1695–1698.
- [40] L. Kubečka, J. Jan, and R. Kolář: Retrospective illumination correction of retinal images. *J. Biomedical Imaging* (2010), 5, 201–210.
- [41] L. Kubečka, J. Jan, R. Kolář, and R. Jiřík: Improving quality of autofluorescence images using non-rigid image registration. In: Proc. EUSIPCO 2006, Florence 2006, CD issue, pp. 357–361.
- [42] L. Kubečka, J. Jan, R. Kolář, and R. Jiřík: Elastic registration for auto-fluorescence image averaging. In: Proc. IEEE-EMBC 2006, New York 2006, CD issue, pp. 1948–1951.
- [43] R. Laemmer et al.: Measurement of autofluorescence in the parapapillary atrophic zone in patients with ocular hypertension. *Graefes Arch. Clin. Exp. Ophthalmol.* (2007), 245, 51–58.
- [44] M. Lalondey, L. Gagnony, and M.C. Boucherz: Non-recursive paired tracking for vessel extraction from retinal images. In: Proc. Vision Interface 2000, Montreal 2000, pp. 61–68.
- [45] S.Y. Lee et al.: Automated quantification of retinal nerve fiber layer atrophy in fundus photograph. In: Proc. IEEE EMBC San Francisco 2004, 1, pp. 1241–1243.
- [46] S.Z. Li et al.: Markov Radnom Field Modeling in Image Analysis. Springer 2009.
- [47] R. Linde et al.: Reproducibility of parapapillary autofluorescence measurement in glaucoma diagnostics. In: Proc. DOG 2005, p. 482.
- [48] B. Likar, J. Derganc, and F. Pernus: Segmentation-based retrospective correction of intensity non-uniformity in multispectral MR images. In: Proc. Conf. Medical Imaging: Image Processing, San Diego (M. Sonka, J.M. Fitzpatrick, eds.), Proc. SPIE 4684 (2002), pp. 1531–1540.
- [49] B. Likar, J. B. Maintz, M. Viergever, and F. Pernus: Retrospective shading correction based on entropy minimization. *J. Microscopy* 197 (2000), 3, 285–295.
- [50] N. Lois, A. S. Halfyard, A. C. Bird, and F. W. Fitzke: Quantitative evaluation of fundus autofluorescence imaged in vivo in eyes with retinal disease. *Br. J. Ophthalmol.* 84 (2000), 741–5.
- [51] M. Lundström and O. J. Eklundh: Computer densitometry of retinal nerve fibre atrophy – a pilot study. *Acta Ophthalmologica* 58 (1980), 4, 639–644.
- [52] F. Maes: Segmentation and Registration of Multimodal Medical Images. PhD. Thesis, Kath. Univ. Leuven 1998.
- [53] J.-F. Mangin: Entropy minimization for automatic correction of intensity nonuniformity. In: IEEE Works. MMBIA, Hilton Head Island 2000, 162–169.
- [54] G. Michelson and M. J. Groh: Screening models for glaucoma. *Curr Opin Ophthalmol.* 12 (2001), 2, 105–11.
- [55] Ch. Muramatsu, Y. Hayashi, A. Sawada et al.: Detection of retinal nerve fiber layer defects on retinal fundus images for early diagnosis of glaucoma. *J. Biomedical Optics* 15 (2010), 1, 1–7.

- [56] R. Nayak et al.: Automated diagnosis of glaucoma using digital fundus images. *J. Med. Syst.* *33* (2009), 337–346.
- [57] H. Niemann et al.: Towards automated diagnostic evaluation of retina images. *J. Pattern Recognition and Image Analysis* *16* (2006), 4, 671–676.
- [58] M. Niemeijer, J. Staal, B. Ginneken et al.: Comparative study of retinal vessel segmentation methods on a new publicly available database. In: *Proc. SPIE Med. Imag.*, San Diego *5370* (2004), p. 648.
- [59] J. Staal et al.: Ridge-based vessel segmentation in color images of the retina. *IEEE Trans. on Medical Imaging* *23* (2004), 4, 501–509.
- [60] J. Odstrčilík, J. Jan, J. Gazárek, and R. Kolář: Improvement of vessel segmentation by matched filtering in colour retinal images. In: *Proc. World Congress on Med. Physics Biomed. Engrg.*, Munich 2009, p. 4.
- [61] J. Odstrčilík, R. Kolář, V. Harabis, J. Gazárek, and J. Jan: Retinal nerve fiber layer analysis via Markov random fields texture modelling. In: *Proc. EUSIPCO 2010*, Eurasip, Aalborg 2010.
- [62] P. Perona and J. Malik: Scale-space and edge detection using anisotropic diffusion. *IEEE Trans. Pattern Analysis Machine Intelligence* *12* (1990), 629–639.
- [63] R. Porter and N. Canagarajah: Robust rotation-invariant texture classification: wavelet, Gabor filter and GMRF based schemes. *IEEE Proc. Vis.-Image Signal Processing* *144* (1997), 3, 180–188.
- [64] P. Scheunders: An orthogonal wavelet representation of multivalued images. *IEEE Trans. Image Processing* *12* (2003), 6, 718–725.
- [65] M. Skokan, A. Skoupý, and J. Jan: Registration of multimodal images of retina. In: *Proc. 24th Conf. IEEE EMBC*, Houston 2002, pp. 1094–1096.
- [66] M. Styner, CH. Brechbuehler, G. Szekely, and G. Gerig: Parametric estimate of intensity inhomogeneities applied to MRI. *IEEE Trans. Med. Imag.* *19* (2000), 3, 153–165.
- [67] J. Tvrđík: Generalized controlled random search and competing heuristic. In: *Proc. 10th Int. Conf. on Soft Computing MENDEL 2004*, pp. 228–33.
- [68] J. Tvrđík: Controlled random search algorithm with alternating heuristics. *AUTOMA* (2002), 1, 54–57.
- [69] A. Viestenz, A. Langenbucher, and C. Y. Mardin: Parapapillary autofluorescence as indicator for glaucoma. *Klin. Monatsbl. Augenheilkd.* *223* (2006), 315–20.
- [70] K. A. Vermeer et al.: A model based method for retinal blood vessel detection. *Computers in Biology and Medicine* *34* (2004), 209–219.
- [71] J. Zhu, B. Liu, and S. C. Schwartz: General illumination correction and its application to face normalization. In: *Proc. IEEE ICASSP'03* *3* (2003), pp. III–133–6.
- [72] B. Zitová and J. Flusser: Image registration methods: a survey image. *Vis. Comput.* *21* (2003), 977–1000.

*Jiří Jan, Department of Biomedical Engineering, FEEC, Brno University of Technology, Kolejní 4, 612 00 Brno. Czech Republic.*

*e-mail: jan@feec.vutbr.cz*

*Radim Kolář, Department of Biomedical Engineering, FEEC, Brno University of Technology, Kolejní 4, 612 00 Brno. Czech Republic.*

*e-mail: kolarr@feec.vutbr.cz*

*Libor Kubečka, Department of Biomedical Engineering, FEEC, Brno University of Technology, Kolejní 4, 612 00 Brno. Czech Republic.*

*e-mail: kubecka@feec.vutbr.cz*

*Jan Odstrčilík, Department of Biomedical Engineering, FEEC, Brno University of Technology, Kolejní 4, 612 00 Brno. Czech Republic.*

*e-mail: odstrcilik@feec.vutbr.cz*

*Jiří Gazárek, Department of Biomedical Engineering, FEEC, Brno University of Technology, Kolejní 4, 612 00 Brno. Czech Republic.*

*e-mail: gazarek@feec.vutbr.cz*